

Numerical Simulation of an Aortic Flow Based on a HLLC Type Incompressible Flow Solver

Yang-Yao Niu^{1,*}, Chih-Hung Chang¹, Wen-Yih I. Tseng²,
Hsu-Hsia Peng² and Hsi-Yu Yu²

¹ Department of Mechanical Engineering, Chung-Hua University, Hsin-Chu, 30067
Taiwan.

² National Taiwan University Hospital, No. 7, Chung-Shan South Road, Taipei,
Taiwan.

Received 25 October 2007; Accepted (in revised version) 1 May 2008

Communicated by Kun Xu

Available online 15 July 2008

Abstract. In this study, a three-dimensional artificial compressibility solver based on the average-state Harten-Lax-van Leer-Contact (HLLC) [13] type Riemann solution is first proposed and developed to solve the time-dependent incompressible flow equations. To implement unsteady flow calculations, a dual time stepping strategy including the LU decomposition method is used in the pseudo-time iteration and the second-order accurate backward difference is adopted to discretize the unsteady flow term. Also a third-order accurate HLLC numerical flux is derived for approximating the inviscid terms. To verify numerical accuracy, flows over a lid-driven cavity and an oscillating flat plate are chosen as the benchmark tests. In addition, the current solver is extended to solve blood flows in a realistic human aorta measured from MRI (Magnetic Resonance Imaging). The simulation geometry was derived from a three-dimensional reconstruction of a series of two-dimensional slices obtained in vivo. Numerical results demonstrate wall stresses were highly dynamic, but were generally high along the outer wall in the vicinity of the branches and low along the inner wall, particularly in the descending aorta. The maximum wall stress distribution is presented on the aortic arch in the systole. In addition, extensive counter-clockwise secondary flows and three-dimensional helical vortex influenced considerably by the presence of vessel contraction, torsion and the branches were shown in the descending aorta in the late systole and early diastolic cycles.

AMS subject classifications: 76D05, 92C35, 74F10

Key words: HLLC, Riemann solver, incompressible flow, aortic flow, fluid-structure interaction.

*Corresponding author. *Email address:* yniu@chu.edu.tw (Y.-Y. Niu)

1 Introduction

One of the popular numerical algorithms for the calculations of incompressible flows is based on Chorin's artificial compressibility method [1]. In recent years, the artificial compressibility strategy has been applied by Pan and Chakravarthy [2], Rogers and Kwak [3], Chen et al. [4], using an implicit line relaxation or LU decomposition scheme in pseudo time and applying Roe type Riemann solver based on high-order upwinding or weighted ENO interpolation on the spatial differencing. The development of the artificial compressibility method has been verified and agreed with several validated data ranging from analytical solutions of simple flows to measured data of complicated transient vortex shedding. However, the computing efficiency of three-dimensional flow problems is still an unsolved issue due to the tedious calculations on the high-order implicit and explicit numerical inviscid and viscous fluxes. To improve numerical efficiency and simplicity, Belov et al. [5] used an explicit artificial compressibility preconditioning with Jameson's artificial viscosity method to construct numerical fluxes for hyperbolic type incompressible flow equations. They utilized second-order backward difference to discretize the physical time term and a rational fourth order Runge Kutta scheme to proceed the subiterations in each pseudo-time step, thus allowing for the computations to march toward a steady state during every physical time step and achieve accurate unsteady flow calculations. In addition to Jameson type explicit preconditioning, Jin and Xu [6,7] recently provide another alternative to simulate the low Reynolds number flow based on gas-kinetic BGK model. Their gas-kinetic solver has been developed in a moving frame on the unified coordinates of Hui [8] and achieved many successful calculations of the flows with free surface and moving boundaries in the incompressible laminar flow regime. However, the applicability of gas-kinetic type solver on the calculations of complex incompressible flows such as vortex shedding or turbulence is still unknown and needs more verification. Up to the present, even so many existing hyperbolic type incompressible flow solvers have been developed, the Roe type approximate Riemann solver may be the most widely used one to solve the artificial compressibility based incompressible equations. In our previous works [9], we have developed a unified artificial compressibility solver based on the Roe type numerical flux under the hybrid Eulerian-Lagrangian coordinates to simulate the moving body flows. Our preliminary results have verified the accuracy and robustness of the unified artificial compressibility solver on many steady and transient cases. However, the Roe type solver is very time-consuming and inefficient, especially on the calculations of the three-dimensional unsteady flow problems.

In this study, we propose an alternative artificial compressibility solver based on average-state HLLC Riemann solutions originated from Toro's theoretical analysis [10]. First, the concept of average-state approximations of Riemann problems was introduced by Harten, Lax, and van Leer [11]. There is a large hierarchy of numerical flux which arises from this approach, all of which may be applied directly to the Euler equations without the need for additional ad hoc modifications. Unfortunately, most of these ap-

proximations appear to be ill suited to the implicit solution of the Navier-Stokes equations. One major problem stems from the inability of the simpler flux models to exactly preserve an isolated contact or shear wave. This results in excessive diffusion of boundary layers, yet also poor convergence rates. Therefore, a clear requirement is to minimize the degree of simplification to a level which does not ruin the numerical accuracy. Against this background, Batten et al. [12] constructed an implicit scheme based on the HLLC Riemann solver of Toro et al. [13], which contains the most detailed physics of any of the average-stage schemes considered. By means of implicit time integration [12], a large tolerance on CFL number restriction is allowed. Based on the previous efforts on HLLC type Riemann solver, we would like to extend it to solve the incompressible flow equations. To capture inherently unsteady physics of incompressible flows, a dual-time implicit formulation containing a second-order accurate backward difference in discretizing unsteady time term and the LU decomposition used in the pseudo-time iteration to approach the steady-state in every physical time step. Also, a third-order HLLC numerical flux [12–14] is derived for approximating the inviscid terms. The validation of the proposed HLLC incompressible solver is performed on the cases of the lid-driven cavity flow [15–17].

In addition, a preliminary simulation of aortic flow is selected in the three-dimensional numerical application. It is well known that aortic dissection, stenosis and aneurysm are widely seen among the vascular diseases. Clinical observations [18–24] show that these arterial diseases can alter blood flow characteristics in arteries significantly. The altered hemodynamics may further influence the development of the disease and arterial deformity. One vascular site within which the fluid mechanical environment is especially complex is the region of the aortic arch and its major branches. From geometrical viewpoint, the centerline of the arch does not lie in a plane, and the severity of the arch distortion is suspected to be closely related to the frequency of aneurysms. Kilner et al. [19] constructed images of human aortas by stacking a series of computed topographical slices, and indicated that the angle between the ascending and descending legs of the arch in the cranial view tends to be a normal aorta case. With regards to blood flow in the aorta, they observed a characteristic flow field that a right-handed helical blood flow prevailed at the top of the arch and a left-handed secondary blood flow located in the descending arch at late systole using MRA measurement. They simulated the large clockwise circulation at the arch, and the large counter-clockwise one at the descending part. The arch is characterized by extensive curvatures, which would be expected to lead to velocity profile skewness as well as to complex secondary flow motions. Furthermore, the three aortic arch branches which emerge in different planes are likely to have a large impact on the flow field. Shahcheragh et al. [24] have pointed that aortic branching and curvatures are attributable to a large degree to the combined effects of complex arterial geometry and flow pulsatility.

From the above described works on aortic flow, the distribution of wall stresses along the thoracic aorta with ascending branch effects is seldom discussed. Also the simulation of blood flowing through the abnormal thoracic aorta and the formation vessel wall stress caused by thoracic aortic disease were not widely documented. Therefore, the es-

timination of wall stress distributions along a normal thoracic aorta and an aortic stenosis with one ascending branch will be highly required. In our previous work [24], numerical results of wall shear stress distributions have been obtained for straight and curved stenosis models. The results demonstrated that the subsequent strong positive-negative oscillations of wall shear stresses behind the stenotic area are found in the case of $Re=400$ and 600 on their outer walls. Also negative maximum wall stresses are found to occur at the upstream of the stenosis on the inner walls. These may correspond to the reattachment locations of the second separation zone behind the stenosis and stronger adverse pressure gradients on the outer wall.

In the further works on the estimations of shear stress on aorta, magnetic resonance imaging in vivo using MRA scan imaging in National Taiwan University Hospital will provide the reconstruction of a realistic normal aorta with three branches from a health young male. The form of the wall stress and blood flow velocity in a health aorta with three branches will be investigated. This paper is organized as follows: Section 2 is the mathematical formulation of the artificial incompressible Navier-Stokes equations in generalized coordinates, and the derived HLLC numerical flux. Section 3 is about numerical modeling. Section 4 presents the results of test cases.

2 Governing equation

The governing equations considered are the nonlinear time-dependent incompressible Navier-Stokes equations of a laminar, constant viscosity flow without body forces. Introducing the pseudo-compressibility to connect pressure with continuity equation based on [1], the equations of motion of the fluid can be compactly written in generalized curvilinear coordinate system as

$$\frac{\partial Q_v}{\partial t} + \frac{\partial Q}{\partial \tau} + \frac{\partial}{\partial \xi}(E - E_v) + \frac{\partial}{\partial \eta}(F - F_v) + \frac{\partial}{\partial \zeta}(G - G_v) = 0, \quad (2.1)$$

where

$$Q = \frac{1}{J} \begin{bmatrix} p \\ u \\ v \\ w \end{bmatrix}, \quad Q_v = \frac{1}{J} \begin{bmatrix} 0 \\ u \\ v \\ w \end{bmatrix}, \quad E = \frac{1}{J} \begin{bmatrix} \beta U + \xi_t(p - \beta) \\ uU + \xi_x p \\ vU + \xi_y p \\ wU + \xi_z p \end{bmatrix},$$

$$F = \frac{1}{J} \begin{bmatrix} \beta V + \eta_t(p - \beta) \\ uV + \eta_x p \\ vV + \eta_y p \\ wV + \eta_z p \end{bmatrix}, \quad G = \frac{1}{J} \begin{bmatrix} \beta W + \zeta_t(p - \beta) \\ uW + \zeta_x p \\ vW + \zeta_y p \\ wW + \zeta_z p \end{bmatrix},$$

and β is the pseudo-compressibility constant, p is the static pressure, u , v , and w are the velocity components in Cartesian coordinates. E_v , F_v and G_v are viscous terms. J is the

Jacobian of the transformation, and U , V and W are the contravariant velocities like

$$\begin{aligned} U &= \zeta_t + \zeta_x u + \zeta_y v + \zeta_z w, \\ V &= \eta_t + \eta_x u + \eta_y v + \eta_z w, \\ W &= \zeta_t + \zeta_x u + \zeta_y v + \zeta_z w. \end{aligned} \quad (2.2)$$

The inviscid flux Jacobian $A = \partial E / \partial Q$ and its four distinct eigenvalues:

$$(\lambda_1, \lambda_2, \lambda_3, \lambda_4) = (U, U, U + C, U - C), \quad (2.3)$$

where $C = \sqrt{U^2 + \beta(\tilde{\zeta}_x^2 + \tilde{\zeta}_y^2 + \tilde{\zeta}_z^2)}$.

3 Numerical approach

3.1 Time integration

To implement the time evolution of the governing equations, usually the physical-time term is discretized using a second-order, three-point, backward difference formula; that is

$$\frac{\partial Q_v}{\partial t} = \frac{1.5Q_v^{n+1,p+1} - 2Q_v^n + 0.5Q_v^{n-1}}{\Delta t}, \quad (3.1)$$

where n designates the index of the physical-time level and p is the index of the artificial-time level. The artificial-time term is discretized by the following implicit Euler finite-difference formula:

$$\frac{\partial Q}{\partial \tau} = \frac{Q^{n+1,p+1} - Q^{n+1,p}}{\Delta \tau}. \quad (3.2)$$

Based on Eqs. (2.3) and (3.1), the linearized governing Eqs. (2.1) can be written as

$$\begin{aligned} & \left(\frac{1.5}{J\Delta t} + \frac{1}{J\Delta \tau} + \frac{\partial A}{\partial \xi} + \frac{\partial B}{\partial \eta} + \frac{\partial C}{\partial \zeta} - \frac{\partial A_v}{\partial \xi} - \frac{\partial B_v}{\partial \eta} - \frac{\partial C_v}{\partial \zeta} \right) \Delta Q^p \\ &= - \frac{1.5Q_v^p - 2Q_v^n + 0.5Q_v^{n-1}}{\Delta t} - \left(\frac{\partial(F - F_v)}{\partial \xi} + \frac{\partial(G - G_v)}{\partial \eta} + \frac{\partial(H - H_v)}{\partial \zeta} \right)^p \\ &= -\text{Res}(Q)^p. \end{aligned} \quad (3.3)$$

The above equation can be factorized using the LU decomposition method for the pseudo time iteration. $\text{Res}(Q)$ is the unsteady residue vector, ΔQ is the spatial difference $Q_{i+1} - Q_i$. $\Delta \tau$ is chosen as the local pseudo time step which is determined by the largest eigenvalue of the preconditioning system of governing equations for each grid cell. The diffusion terms are evaluated by the standard central differencing scheme. The implicit part at the left-hand side of Eq. (3.3) is discretized using a first-order upwind difference scheme. One of them in the ξ direction can be expressed such as:

$$\frac{\partial A}{\partial \xi} = \frac{(A_{i+1,j,k} - A_{i,j,k})}{\Delta \xi}, \quad (3.4)$$

where $A = A^+ + A^-$. A^+ and A^- are computed based on the eigenvalues of the matrix A and the related eigenvector T and its inverse T^{-1} like

$$A^\pm = T\Lambda^\pm T^{-1}, \quad (3.5)$$

where $\Lambda = \text{diag}(\lambda_1, \lambda_2, \lambda_3, \lambda_4, \lambda_5)$. Similarly as B and C . Eq. (3.3) can be factored after using finite difference formulation for the derivative term as

$$(D-L)D^{-1}(D+U)\Delta Q_{i,j,k}^{n+1,k+1} = J\Delta\tau \text{Res}(Q)^{n+1,k} \quad (3.6)$$

where L , D and U are determined recursively as:

$$\begin{aligned} L = & \frac{\Delta\tau}{\Delta\xi} \left[-A_{i-1,j,k}^+ + \frac{1}{2}(A_v)_{i-1,j,k} \right] + \frac{\Delta\tau}{\Delta\eta} \left[-B_{i,j-1,k}^+ + \frac{1}{2}(B_v)_{i,j-1,k} \right] \\ & + \frac{\Delta\tau}{\Delta\xi} \left[-C_{i,j,k-1}^+ + \frac{1}{2}(C_v)_{i,j,k-1} \right], \end{aligned} \quad (3.7)$$

$$\begin{aligned} D = & I + \frac{3\Delta\tau}{2\Delta t} + \frac{\Delta\tau}{\Delta\xi} \left[A_{i,j,k} - \frac{1}{2}(A_v)_{i,j,k} \right] + \frac{\Delta\tau}{\Delta\eta} \left[B_{i,j,k} - \frac{1}{2}(B_v)_{i,j,k} \right] \\ & + \frac{\Delta\tau}{\Delta\xi} \left[C_{i,j,k} - \frac{1}{2}(C_v)_{i,j,k} \right], \end{aligned} \quad (3.8)$$

$$\begin{aligned} U = & \frac{\Delta\tau}{\Delta\xi} \left[A_{i+1,j,k}^+ - \frac{1}{2}(A_v)_{i+1,j,k} \right] + \frac{\Delta\tau}{\Delta\eta} \left[B_{i,j+1,k}^+ - \frac{1}{2}(B_v)_{i,j+1,k} \right] \\ & + \frac{\Delta\tau}{\Delta\xi} \left[C_{i,j,k+1}^+ - \frac{1}{2}(C_v)_{i,j,k+1} \right]. \end{aligned} \quad (3.9)$$

Furthermore, Eq. (3.6) can be computed using the LU approach for advance the solution in pseudo-time is implemented in two steps a backward and forward step in each direction as: First

$$(D-L)\Delta Q^* = RHS_{i,j,k}^{n+1,k+1/2}. \quad (3.10)$$

Then

$$(D+U)\Delta Q_{i,j,k}^{n+1,k+1} = D\Delta Q^*. \quad (3.11)$$

Finally, the primitive variables at the new pseudo-time level $k+1$ is then updated by

$$Q_{i,j,k}^{n+1,k+1} = Q_{i,j,k}^{n+1,k} + \Delta\hat{Q}^*. \quad (3.12)$$

3.2 HLLC numerical flux

As noted in [11–14] and shown in Fig. 1, the structure of the analytical solution of one-dimensional Riemann problem contains three wave families separating four constant states from left to right states as Q_L , Q_L^* , Q_R^* , Q_R . These states Q_L^* , Q_R^* emerge from the interaction of the data states Q_L^* , Q_R^* and compose the so-called the star Region. The left

and right waves are either shock or rarefaction denoted as the two acoustic waves S_L and S_R seen in Fig. 1; all flow quantities change across these waves, the change being discontinuous across shocks. The middle wave is always a shear wave S_M across which Q_L^* , Q_R^* . The solution strategy is based on the fact that both Q_L^* and Q_R^* are constant throughout the star region.

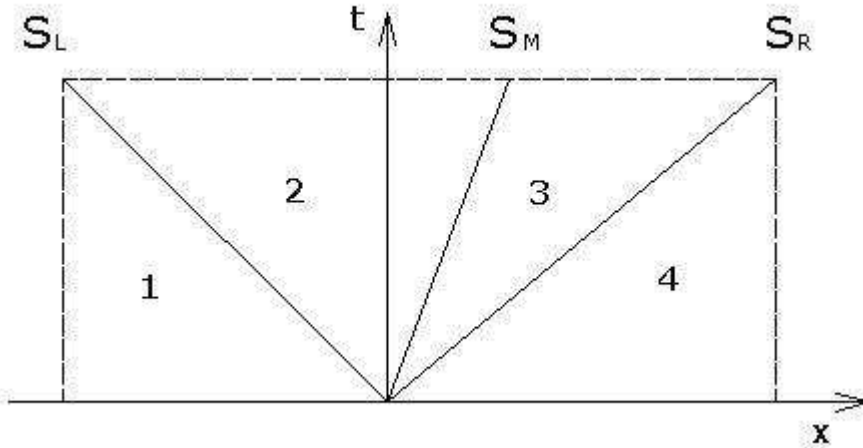


Figure 1: A structure of wave patterns of one-dimensional Riemann problem.

Harten et al. [11] proposed various simplifications to the internal structure of the Riemann fan by taking integral averages of the conserved variables over sections of the fan. The most elaborate solver suggested by Harten et al. [11] is a two-state HLL approximation in which two-state averages are computed, one from the left-most acoustic wave to the contact wave and one from the contact to the right-most acoustic wave: The detail of this scheme are rather cumbersome. Harten, Lax and van Leer also proposed an approximated Riemann-solver to find a inviscid flux vector E^* in the star region. However, Toro' HLLC [13] showed that a significant simplification could be made by assuming the particle velocity to be constant across the Riemann fan. Moreover, Batten et al. [12] have shown that, with a suitable choice of all wave speeds. Toro et al.'s two-state HLLC solver resolves isolated shock and contact/shear waves exactly and is positively conservative in the definition of Einfeldt et al. [14] split the star flux E_L^* and E_R^* based on states Q_L^* , Q_R^* . This version of the HLLC type fluxes will be defined as the followings.

The HLLC flux considers two averaged intermediate states, Q_L^* , Q_R^* separated by the contact wave, whose speed is denoted by S_M as seen in Fig. 2. The two-state approximate Riemann solution was defined by Harten et al. [11] as

$$Q_{HLLC} = \begin{cases} Q_L & \text{if } S_L > 0, \\ Q_L^* & \text{if } S_L \leq 0 \leq S_M, \\ Q_R^* & \text{if } S_M \leq 0 \leq S_R, \\ Q_R & \text{if } S_R < 0. \end{cases} \quad (3.13)$$

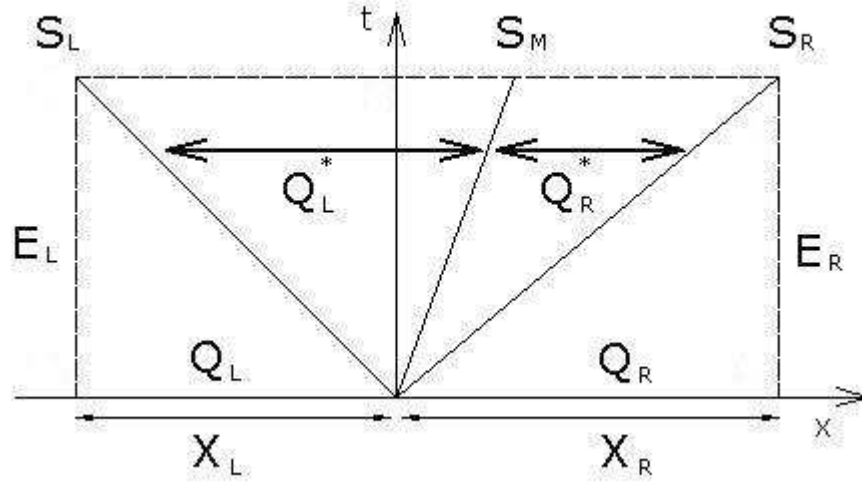


Figure 2: A two-intermediate wave pattern of one-dimensional Riemann problem.

The corresponding interface flux, denoted as F_{HLLC} , is

$$E_{HLLC} = \begin{cases} E_L & \text{if } S_L > 0, \\ E_L^*(Q_L^*) & \text{if } S_L \leq 0 \leq S_M, \\ E_R^*(Q_R^*) & \text{if } S_M \leq 0 \leq S_R, \\ E_R & \text{if } S_R < 0. \end{cases} \quad (3.14)$$

Harten et al. suggested various ways of the exact solutions Q^* between two acoustic waves. The HLLC flux is a modification of HLL. Instead of a single intermediate state Q^* , two intermediate states, Q_L^* and Q_R^* , are assumed, separated by an interface moving with the speed S_M . To calculate Q_L^* and Q_R^* , we recap the approach taken by Batten et al. by applying the Rankine-Hugoniot conditions across the shear wave. However, the simplest approach for computing these star states was suggested by Toro et al., who ignored the influence of expansion fans and made the particle velocity constant between the acoustic waves. Applying the Rankine-Hugoniot condition across the S_L and S_R waves gives

$$\begin{aligned} E_L^* &= E_L + S_L(Q_L^* - Q_L), \\ E_R^* &= E_R + S_R(Q_R^* - Q_R), \end{aligned} \quad (3.15)$$

where S_L, S_R are taken from Einfeldt et al. [14] as $S_L = U_L - C_L$ and $S_R = U_R - C_R$. Based on Eq. (3.6), the rearrangement of the left-side flux of star region, we can obtain $S_L Q_L^* - E_L^* = S_L Q_L - E_L$, namely,

$$S_L \begin{bmatrix} P_L^* \\ u_L^* \\ v_L^* \\ w_L^* \end{bmatrix} - \begin{bmatrix} \beta U_L^* \\ u_L^* U_L^* + P_L^* \zeta_x \\ v_L^* U_L^* + P_L^* \zeta_y \\ w_L^* U_L^* + P_L^* \zeta_z \end{bmatrix} = S_L \begin{bmatrix} P_L \\ u_L \\ v_L \\ w_L \end{bmatrix} - \begin{bmatrix} \beta U_L \\ u_L U_L + P_L \zeta_x \\ v_L U_L + P_L \zeta_y \\ w_L U_L + P_L \zeta_z \end{bmatrix}. \quad (3.16)$$

Furthermore, the speed S_M of the shear wave can be considered as a constant U^* which is the average directed velocity between the two acoustic waves like

$$S_M = U_L^* = U_R^*. \quad (3.17)$$

Then the system Eqs. (3.7) can be rewritten and separated as

$$P_L^* = P_L + \frac{\beta(S_M - U_L)}{S_L}, \quad (3.18)$$

$$u_L^* = \frac{u_L(S_L - U_L)}{S_L - S_M} + \frac{(S_M - U_L)\xi_x\beta}{(S_L - S_M)S_L}, \quad (3.19)$$

$$v_L^* = \frac{v_L(S_L - U_L)}{S_L - S_M} + \frac{(S_M - U_L)\xi_y\beta}{(S_L - S_M)S_L}, \quad (3.20)$$

$$w_L^* = \frac{w_L(S_L - U_L)}{S_L - S_M} + \frac{(S_M - U_L)\xi_z\beta}{(S_L - S_M)S_L}. \quad (3.21)$$

Then the conserved variables at the left-hand side of the star region is rearranged as

$$Q_L^* = \left[P_L + \frac{\beta(S^* - u_L)}{S_L}, S^*, v_L \frac{(S^* - u_L)}{(S_L - S_L)}, w_L \frac{(S^* - u_L)}{(S_L - S_L)} \right]^T \quad (3.22)$$

with

$$S^* = \frac{S_R S_L (P_R - P_L)}{\beta(S_R - S_L)} + \frac{S_R u_L - S_L u_R}{S_R - S_L}. \quad (3.23)$$

The same procedure can be working for the construction of Q_R^* .

3.3 Flux extrapolation

To achieve the high-order accurate flux approximation, one of possibility can be relied on third-order flux extrapolations for the derivatives $\partial_{\xi} E$ like the work in [3]. A third order accurate numerical flux at cell interface is defined by

$$E_{i+\frac{1}{2}} = \frac{1}{2}[E(Q_{i+1}) + E(Q_i)] + \frac{1}{6}[\Delta E_{i-\frac{1}{2}}^+ - \Delta E_{i+\frac{1}{2}}^+ + \Delta E_{i+\frac{1}{2}}^- - \Delta E_{i+\frac{3}{2}}^-], \quad (3.24)$$

where ΔE^{\pm} are the fluxes of the positive and negative traveling waves across cell interfaces. For the HLLC type numerical flux, the flux difference is taken as

$$\Delta E_{i+\frac{1}{2}}^- = E_{i+\frac{1}{2}}^{hllc} - E_i, \quad \Delta E_{i+\frac{1}{2}}^+ = E_{i+1} - E_{i+\frac{1}{2}}^{hllc}. \quad (3.25)$$

3.4 Wall model

In this work, we will simulate blood flows through a deformable aorta as the three-dimensional numerical test. The fluid-structure interaction is required to consider in the numerical implementation. Here, the wall compliance is modeled using an independent ring model [20] to compute the vessel deformations. This model assumes that the structural nodes move only in the radial direction. In spite of its intrinsic limitations, the extreme simplicity of this model makes it very popular. The linear elastic model equation used here is to describe the wall motion as a damped oscillator like

$$m \frac{\partial^2 r}{\partial t^2} + d \frac{\partial r}{\partial t} + kr = P_w, \quad (3.26)$$

where

$$m = \rho_w h, \quad k = \frac{Eh}{(1-\nu^2)a^2}, \quad d = 2\sqrt{mk}$$

and h is the wall thickness, ρ_w the wall density, E the Young's modulus, ν the Poisson ratio, a the vessel radius, r the wall displacement and p_w the pressure force at the wall. The radial displacement of each structural node can be obtained by solving Eq. (3.26) using a fourth-order Runge-Kutta scheme. The fluid-structure Eqs. (3.3) and (3.26) are solved in an uncoupled way. Both the solutions of fluid and structure equations are updated in an unsteady time marching manner. First, the pressure loads at the vessel wall predicted by the fluid solver are transferred to be the source term in the structure equation at the same time step. After that, the wall displacement is updated at each grid point along the whole vessel surface by solving the structure equation. Next, the wall mesh velocities are estimated by a second-order accurate estimation of wall displacements obtained from during the previous two time steps. Finally, the flow variables are updated by the fluid solver based on the new grid points with the mesh velocity. And the updated wall pressure loads are used as the source term of the structure equation for the next time step. The above procedure of the fluid-structure coupling is required to repeat in each subiteration until mass conservation criteria is satisfied in every physical time step, then a cycle of fluid-structure interaction is completed. However, the strategy of the moving grid approach is inclined to produce excessive numerical errors due to the grid torsion. To avoid numerical instability, keeping geometry conservation and grid regeneration may be necessary in every unsteady time stepping of the calculations.

4 Validated cases and discussions

4.1 Lid driven cavity

The lid-driven cavity flow problem is a widely used benchmark test for the incompressible Navier-Stokes code validation. With the simplicity of geometry, the driven cavity flow contains complicated flow physics driven by multiple counter rotating vortices on

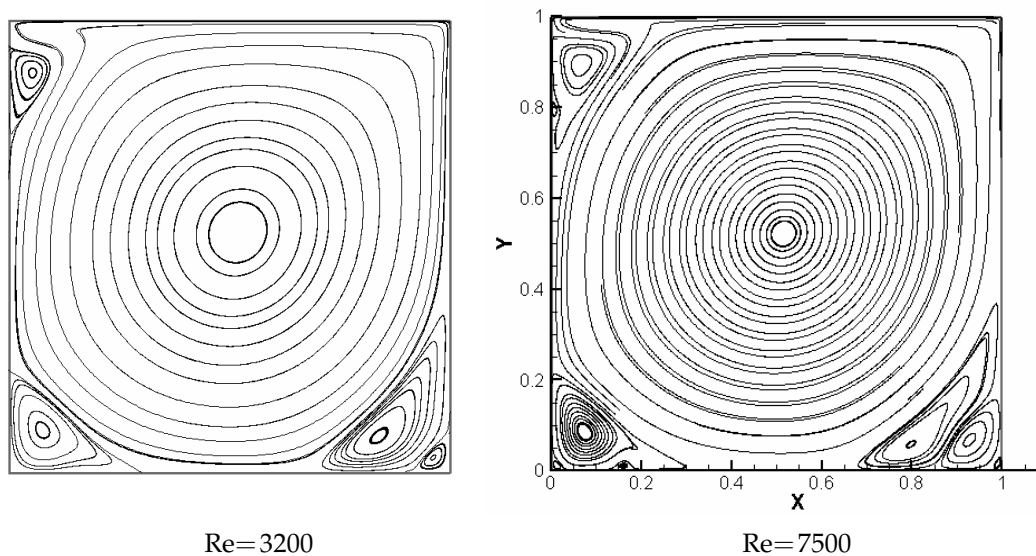


Figure 3: Streamline patterns for lid driven cavity flow.

the corners of the cavity depending on the Reynolds number. A very detailed discussion on computational as well as experimental studies on the lid-driven cavity flow can be found in Shankar & Deshpande [15] and S. Garcia [16]. As noted in their studies, different numerical method solutions found in the literature agree with each other at low Reynolds numbers ($Re=1,000$). However, the solutions at higher Reynolds numbers ($Re > 7500$) have noticeable discrepancies. Nevertheless there still are very different results concerning the first Hopf bifurcation and the behavior of the solution for intermediate and high Reynolds numbers as seen in most of former works [15, 16]. It was suggested that the first Hopf bifurcation occurs around Reynolds number $Re=7500$. To avoid the unnecessary controversy validated data, the driven cavity flow with Reynolds number 3200 and 7500 as seen in the works of Ghia [17] et al. are chosen to verify numerical accuracy.

From all our comparisons we can conclude that even for $Re=1,000$ higher order approximations together with the use of fine grids are necessary for accuracy. The grid independence study is necessary. The computations are performed on a 118×118 and 236×236 grid systems which are clustered near the wall and stretched from the wall to the cavity center. Both computed results on the two grid meshes are close. Here, the results on the coarse meshes are demonstrated. The streamtrace patterns in the driven cavity flow are plotted in Fig. 3. It is shown that one primary vortex near the center and three corner eddies are captured. Also one small secondary zone in the lower right corner is visible. Fig. 3 exhibits the formation of the counter-rotating secondary vortices which appear as the Reynolds number increases. It is evident that as the Reynolds number increases, the center of the primary vortex moves towards the geometric center of the cavity. In Fig. 4, the computed u along vertical lines and v velocity along horizontal lines through the center are shown to agree with the validated data.

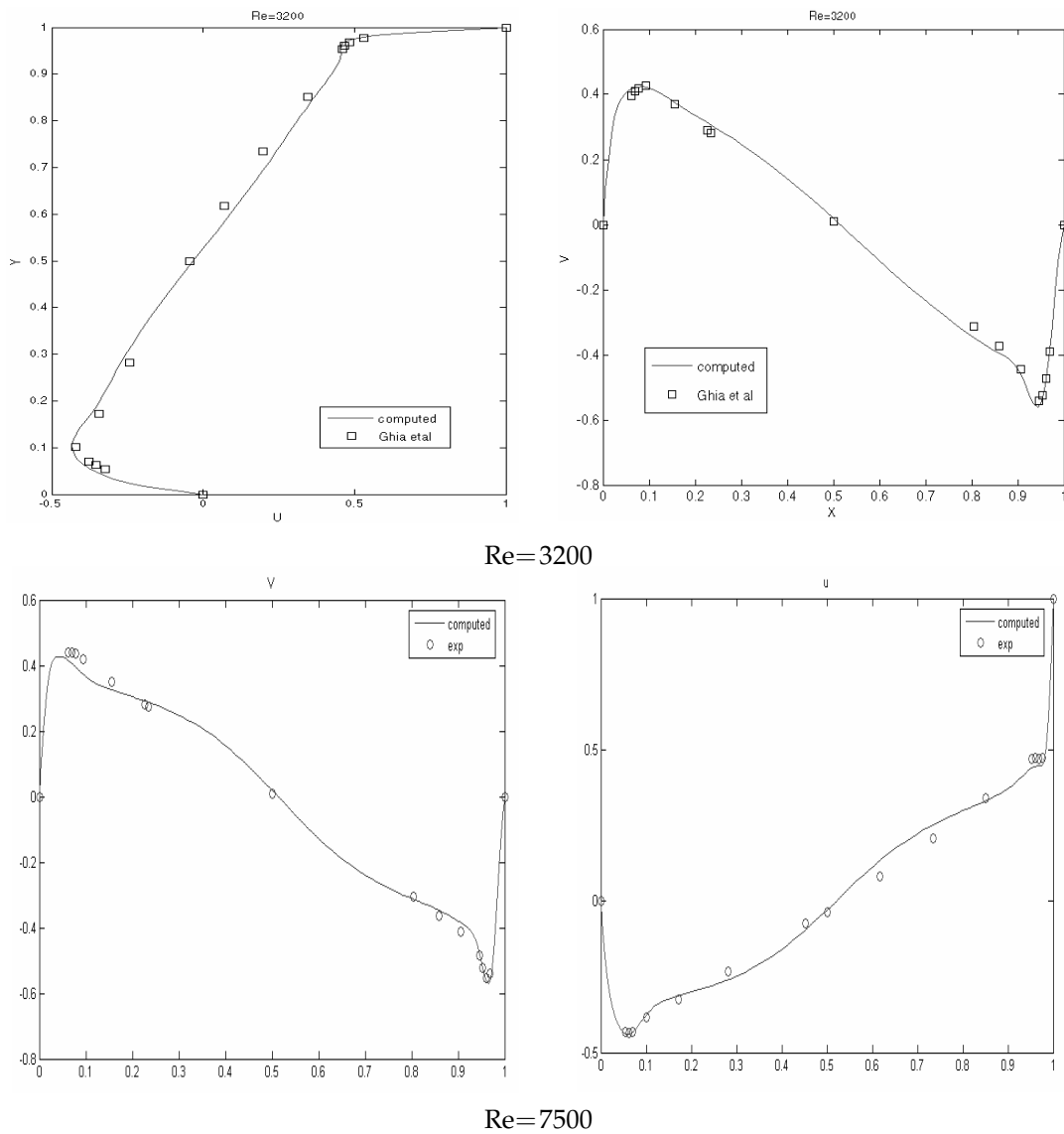


Figure 4: U velocity component along vertical centerline (left); V velocity component along horizontal centerline (right) for the driven cavity flow.

4.2 Aortic flow

In this study, we would like to extend the current HLLC type artificial compressibility solver to simulate blood flows in a realistic human aorta measured by MRA (Magnetic Resonance Imaging) provide by National Taiwan University Hospital for a Reynolds number of 4700 at entrance. The simulation geometry was derived from a three-dimensional reconstruction of a series of two-dimensional slices obtained in vivo. The MRA

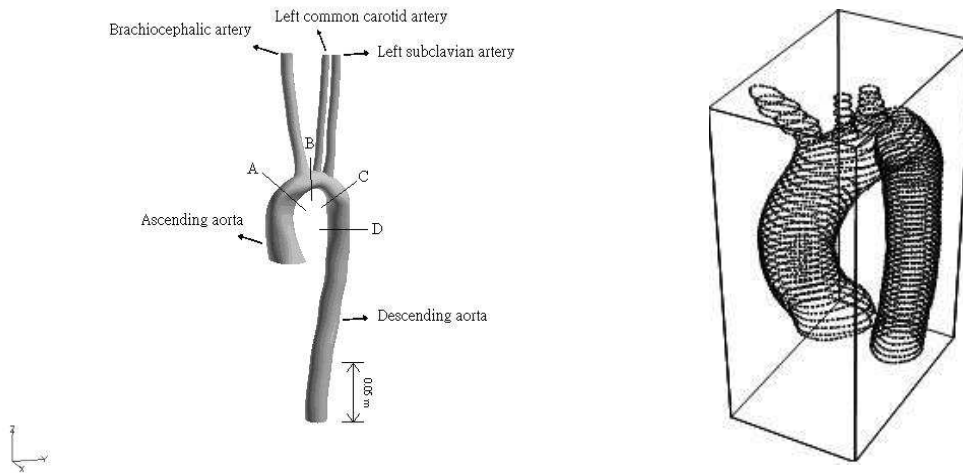


Figure 5: Schematic diagram of a normal aorta with 3 branches (left), aorta outline reconstructed from by MRI (right).

scan consisted of 20 aortic slices in the main aorta and 5 slices in each bifurcation, and the cross-sectional area of the slices were approximated well as non-uniform circles. The centerline data for the circles was determined directly from the MRA scans, and this centerline data was filtered for small wavelength variations with the use of cubic spline-fitting. Those data were curve-fitted to the cubic spline function, and the cross sectional grids were generated on the normal planes defined by the principal normal and binormal at discrete equidistant points along the centerline curve. Using this cross section definition, a computable model can be constructed because adjacent cross sections never overlap if the tube radius is smaller than that of curvature at the local point. A similar procedure was used for the three major aortic branches; however the resolution of the MRA scan data was not as fine as the main aortic arch. The cross-sectional areas of both the aortic section and the branches decreased considerably in the direction of flow. Therefore, an assumption of constant cross-sectional area along the length of the vessels is used for the branches. From the reconstructed model shown in Fig. 5, we assume that the diameters of the aortic arch, the brachiocephalic artery, the left carotid artery, and the left subclavian artery are 2 cm, 1 cm, 0.7 cm, and 0.7 cm, respectively. Three-dimensional 660000 volume meshes were generated for the current aorta model with the following four separated computational meshes employed: one for the region spanning the ascending thoracic aorta along with the aortic arch and a portion of the descending thoracic aorta, and one for each of the three arch branches—the brachiocephalic, left common carotid, and left subclavian arteries. The lengths of the branches were chosen by numerical experiments to be long enough that there was no dependence of the flow at the inlet of the branches on the branch exit boundary conditions.

To perform numerical simulation, one cycle of heartbeats is 0.855 seconds according

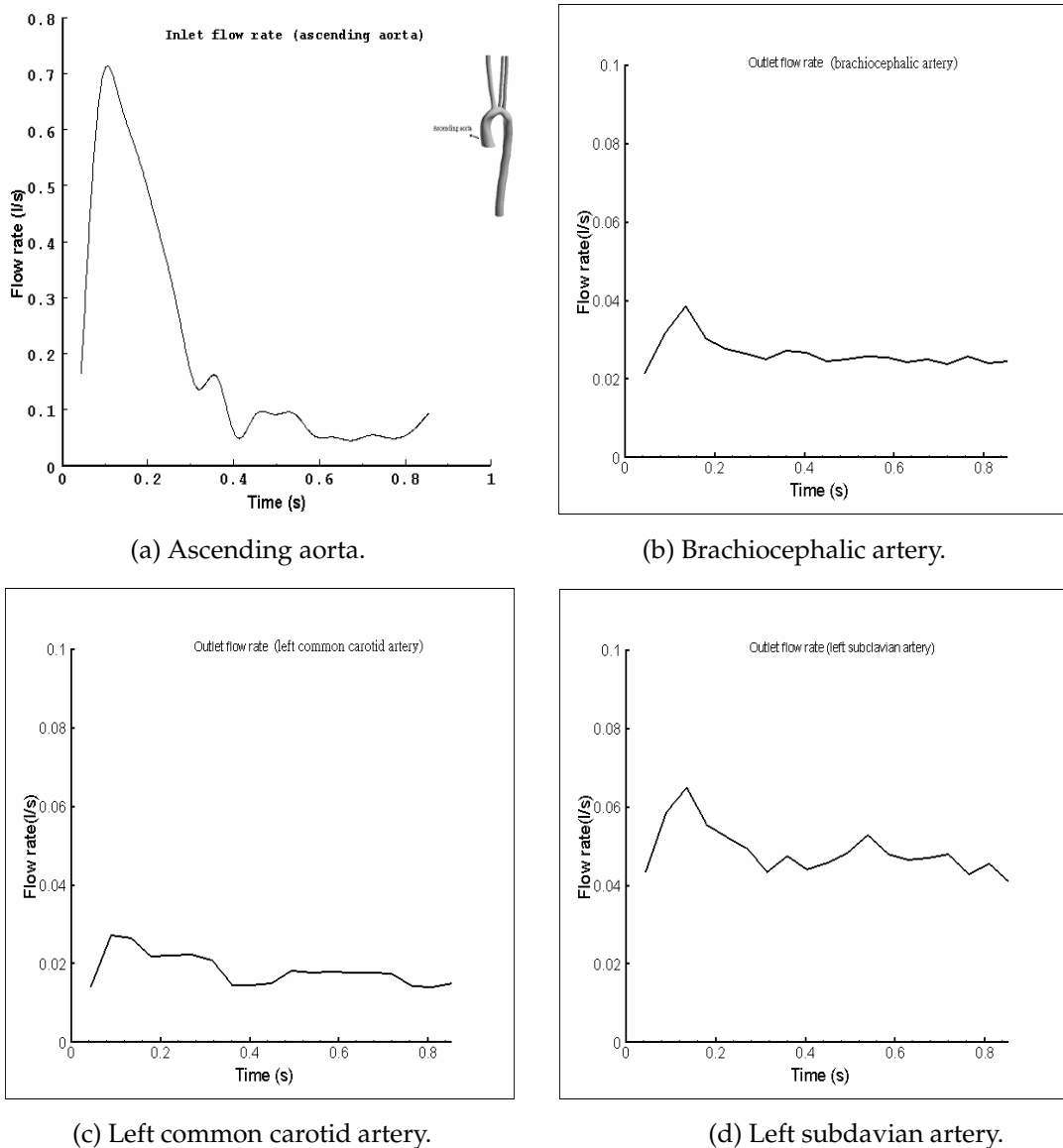


Figure 6: An inlet flow rate measured from MRA.

to MRI data. Eq. (3.3) was solved for a peak Reynolds number of 4700 at the inlet of ascending of aorta and numerical boundaries were chosen based on flow conditions: (i) MRA scan flow rate at the inlet of ascending aorta as shown in Fig. 6(a). (ii) Surface traction free and zero velocity gradients at the outlet of descending aorta. (iii) MRA scan flow rates at the outlet of three branches as shown in Figs. 6(b)-6(d). (iv) Grid velocity as the vessel wall velocity condition. The computed residues were set to satisfy the convergence criterion in the calculations of equation. (v) And the final results were achieved at

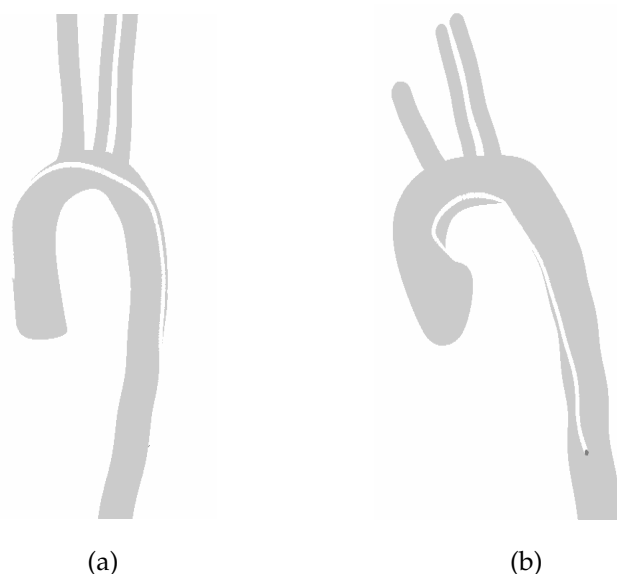


Figure 7: A description of the line (a) with greater curvature (outer wall) and the line (b) with less curvature (inner wall) along the aortic arch.

the fifth cycle of the computation which was starting from the initial conditions as zero velocity. Pressure and shear stress distributions on vessel walls and secondary flows on the cross sections of the aorta are shown in our computations.

First, the wall stress and pressure distributions on the greater curvature and the lesser curvature of the aorta as defined in Fig. 7 are observed. In our numerical results, Fig. 8 presents the pressure distributions on vessel walls of the aorta in a pulsatile cycle. We can find that the pressures were higher along the greater curvature of the aorta, and were lower along the lesser curvature in the systole. A high pressure distribution on the greater curvature may be resulted from a direct impact of strong flow inertia momentum in the increased inlet flow rate. Because the inlet flow rate approaches zero in the late diastole, the pressure has been very nearly the same in the lesser curvature and greater curvature. It is obvious that the pressures drop at the aortic arch and downstream of the aortic arch at $t = 2/19T$ and $4/19T$. That may be caused by the appearance of descending vessel contraction and dilation and influenced by the presence of the bifurcations.

Fig. 9 presents the wall shear stress distributions. It is observed that there is a computed peak value of the wall shear stress along the aortic wall at the aortic arch and the wall shear stress drop at downstream of the aortic arch during $t = 2/19T$ and $t = 4/19T$. These phenomena may be resulted from the variation of the vessel diameter and the presence of the bifurcation. The inlet flow rate approaches zero in the late diastole, so the wall shear stress distributions are shown to be similar as the values on the lesser curvature and greater curvature. It demonstrates that wall shear stresses were highly dynamic, but were generally high along the greater curvature in the vicinity of the branches and low along

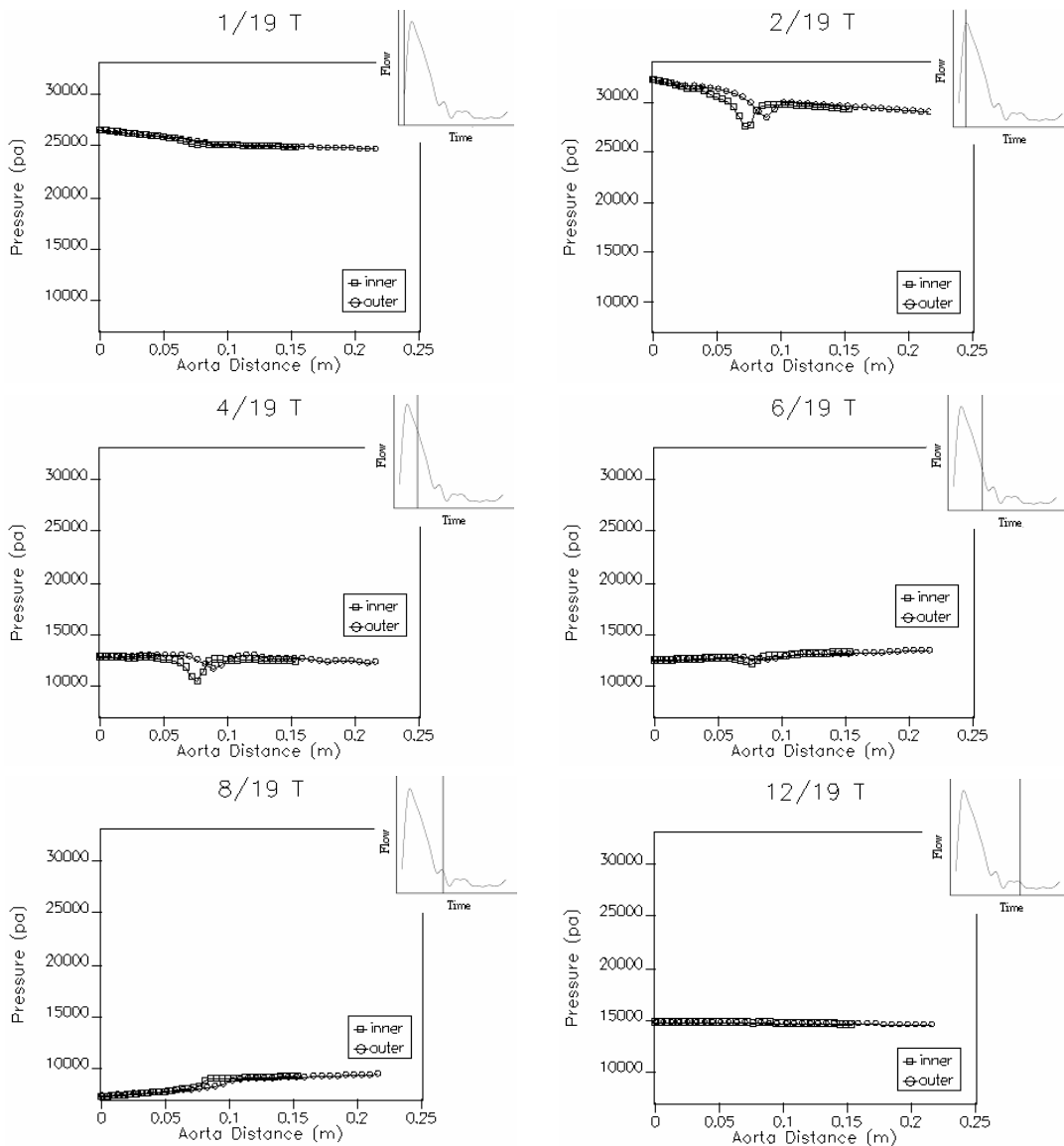


Figure 8: Pressure distributions in a pulsatile cycle (\square -outer wall, \circ -inner wall).

the lesser curvature, particularly in the descending thoracic aorta. The maximum wall shear stress distribution is presented on the aortic arch in the late systole.

A diagram of each cross section in aortic arch is demonstrated and defined in Fig. 10. A, B, C are located in ascending aorta and E, F, G, H are located in descending aorta. The cross section D is located in aortic arch. As shown in Fig. 10, extensive secondary flow motions are observed in the cross section D, F, G, H as $t = 7/19T$ and $9/19T$, and the structures of these secondary flows are seen around the area of the branches. Also,

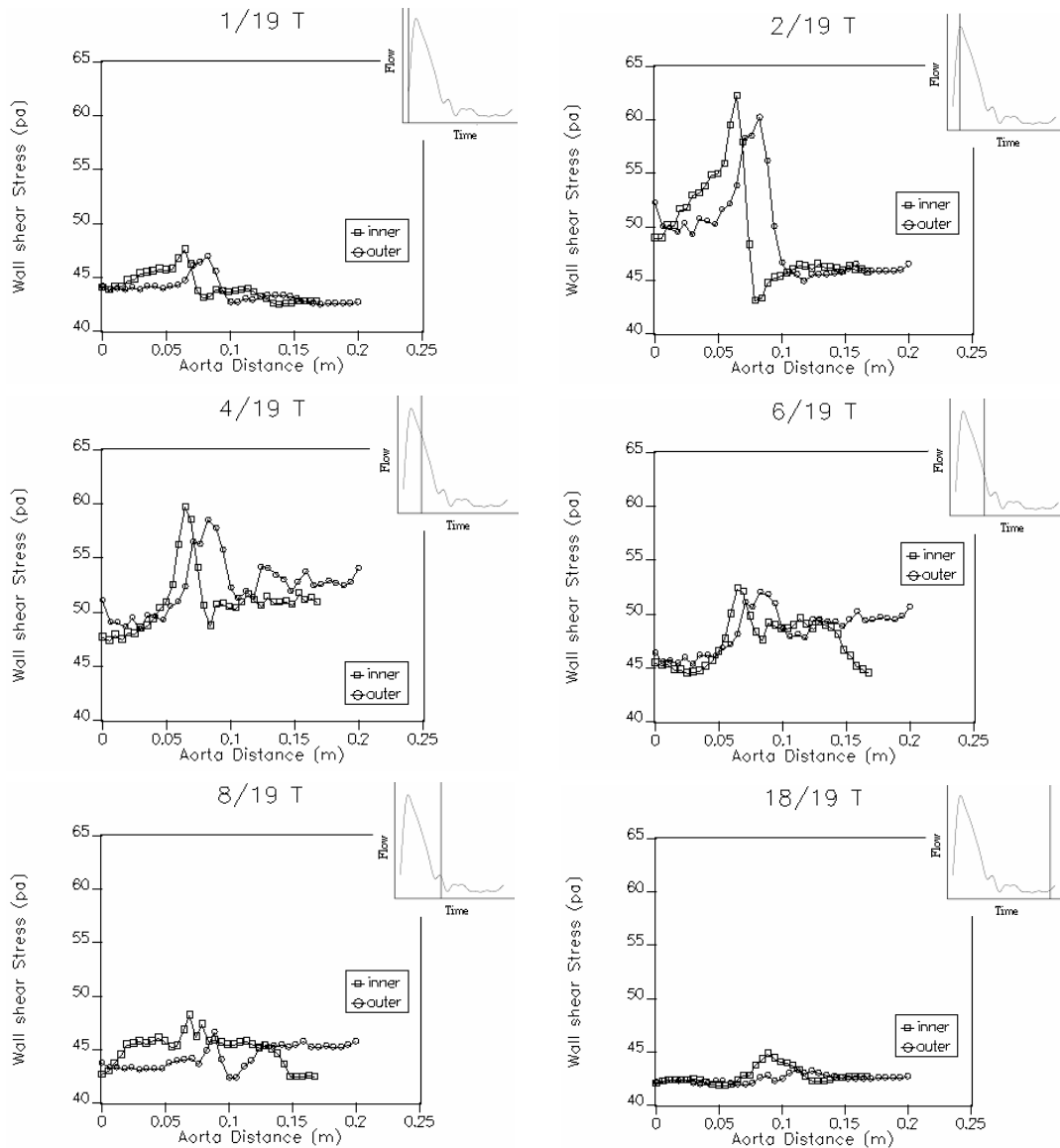


Figure 9: Wall shear stress distributions in a pulsatile cycle (\square -outer wall, \circ -inner wall).

it is observed that clockwise secondary flow recirculation appears in the downstream of aortic arch in the late systole and turn out to be a pair of counter-clockwise vortex appearing in the turning corner of the aortic arch in the early diastole. However, the counter-clockwise vortex disappears in the upstream of the aortic arch and moves to the downstream of the descending aorta in the late diastole. These above predicted results are comparably consistent with previous experimental measurements of Kilner et al. [19]. In addition, the clockwise vortex appears at the ascending parts A-C only seen during the

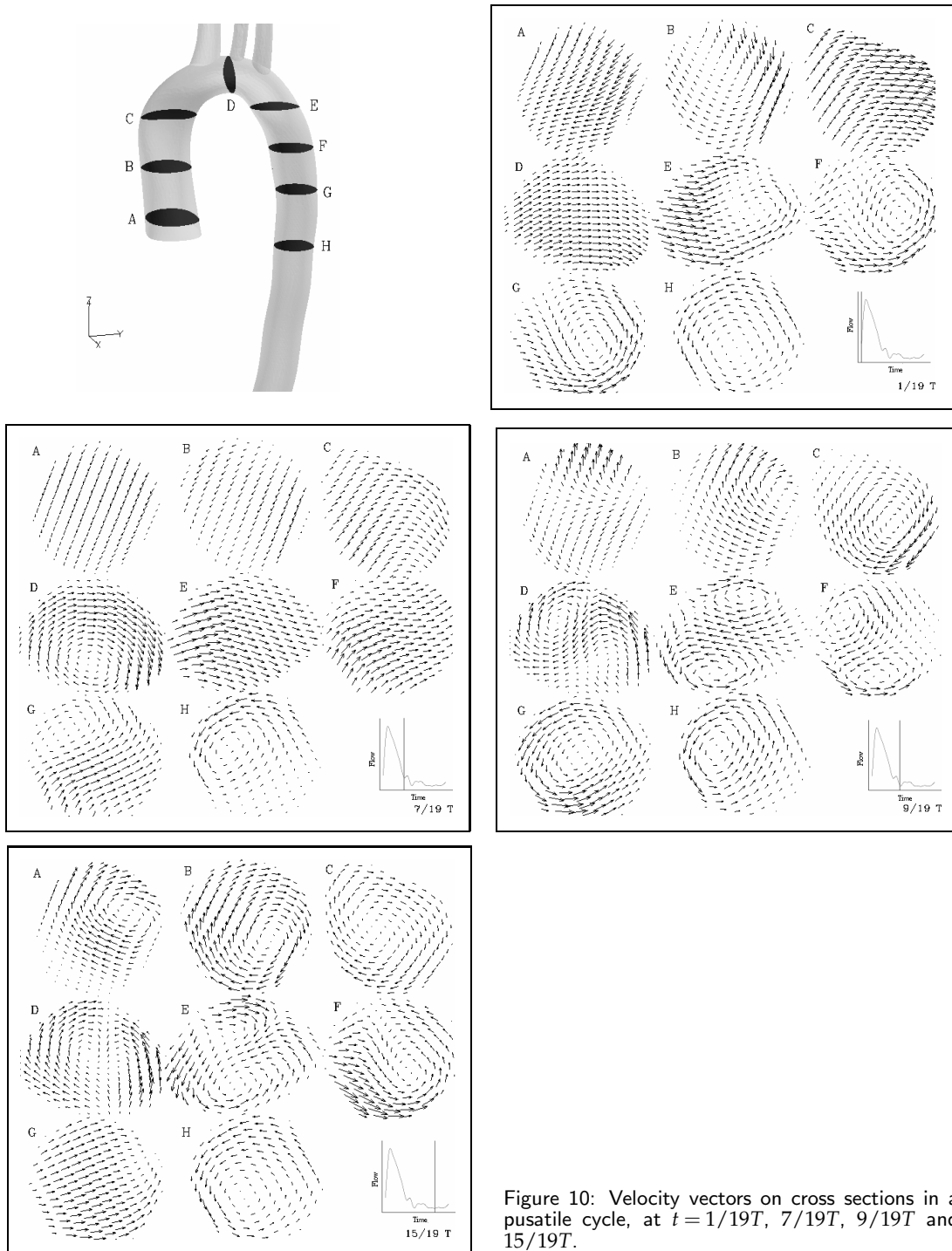


Figure 10: Velocity vectors on cross sections in a pusatile cycle, at $t = 1/19T$, $7/19T$, $9/19T$ and $15/19T$.

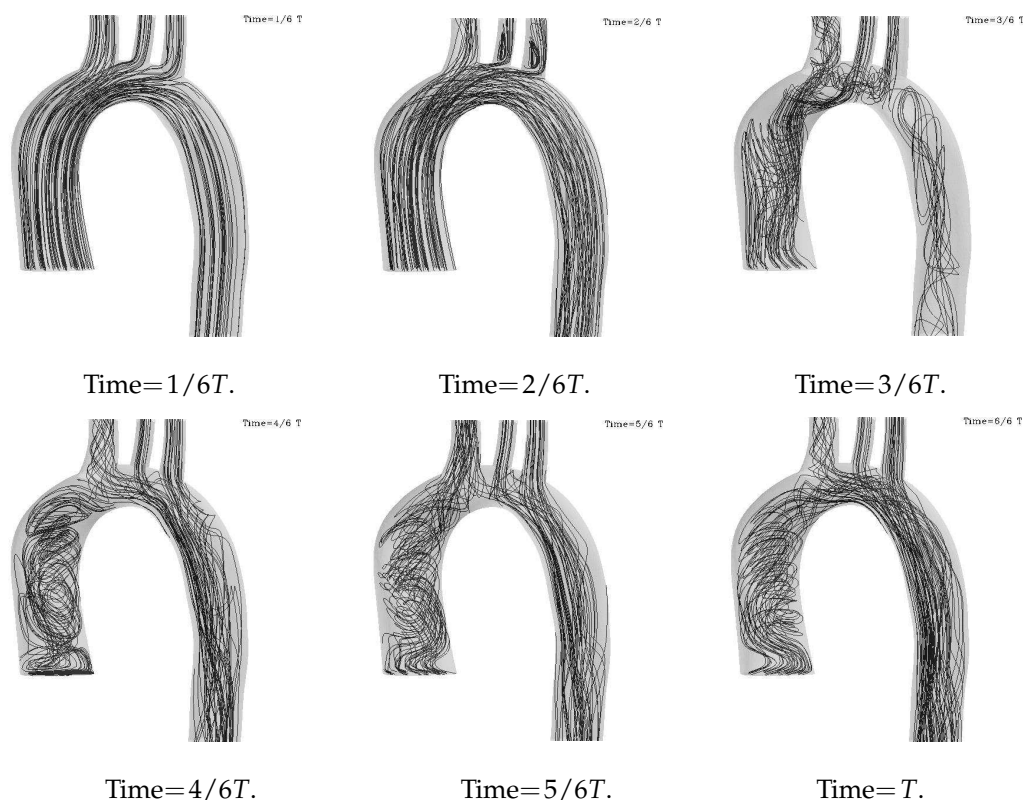


Figure 11: Particle traces along the aorta with three branches in a pulsatile cycle.

diastole. For the three-dimensional observations of predicted flow patterns, the particle traces along the aorta with 3 branches during the whole cycle are shown in Fig. 11. It is observed that secondary flow appears in the left carotid artery and left subclavian artery at $t = 2/6T$. Also we can observe that the vortex existing in the left carotid artery and left subclavian artery disappears at $t = 3/6T$. However, the flow in the brachiocephalic artery becomes a helical type flow motion from $t = 3/6T$ to $t = 4/6T$. The helical type flow rotation is getting declined as the cycle approaches the late period of diastolic cycle.

5 Concluding remarks

In this paper, a transient artificial compressibility solver based on HLLC type Riemann solver is proposed and developed. Numerical validation has been performed against the driven cavity flow, an oscillating plate flow. Also, application is performed on the calculations of an aortic flow based on MRI data including a realistic morphology of the aorta and the inlet and outlet flow rates of blood vessels. The preliminary results of the aortic flow include

1. Wall shear stresses were highly dynamic, but were generally high along the greater

curvature in the vicinity of the branches and low along the lesser curvature. The maximum wall shear stress distribution is presented on the aortic arch in the systole;

2. Clockwise secondary flow recirculation appears in the downstream of aortic arch in the late systole and turn out to be a pair of counter-clockwise vortex appearing in the turning corner of the aortic arch in the early diastole. However, the counter-clockwise vortex disappears in the upstream of the aortic arch and moves to the downstream of the descending aorta in the late diastole;

3. Minor three-dimensional secondary flows appear in second and third branch and flow separation occurs in right branch in the late systole;

4. Extensive secondary flow motion and three-dimensional helical vortex influenced considerably by the presence of vessel contraction, torsion and the branches were shown in the descending aorta in the diastolic cycle.

In the future studies, a non-linear modeling of wall motion for aortic vessel will be considered. The information about material properties of blood vessel especially, in the vicinity of the aortic arch bifurcations, is highly required.

References

- [1] A. J. Chorin, A numerical method for solving viscous flows problems, *J. Comput. Phys.*, 2 (1967), 12-16.
- [2] D. Pan and S. R. Chakravarthy, Unified formulation for incompressible flows, *AIAA paper*, Jan. (1989), 89-0122.
- [3] S. E. Roger and D. Kwak, Upwind differencing scheme for the time-accurate incompressible Navier-Stokes equations, *AIAA J.*, 28(2) (1990), 253-262.
- [4] Yih-Nan Chen, Shih-Chang Yang and Jaw-Ywn Yang, Implicit Weighted essentially non-oscillatory schemes for the incompressible Navier-Stokes equations, *Int. J. Numer. Meth. Fluids*, 31 (1999), 747-765.
- [5] A. Belov, A. Jameson and L. Martinelli, Three-dimensional unsteady incompressible flow calculations using multigrid, *AIAA paper*, (1997), 97-0443.
- [6] C. Jin and K. Xu, A unified moving grid gas-kinetic method in Eulerian space for viscous flow computation, *J. Comput. Phys.*, 222 (2007), 155-175
- [7] C. Jin and K. Xu, Numerical study of the unsteady aerodynamics of freely falling plates, *Commun. Comput. Phys.*, 3 (2008), 834-851.
- [8] W. H. Hui, The unified coordinate system in computational fluid dynamics, *Commun. Comput. Phys.*, 2 (2007), 577-610.
- [9] Y.-Y. Niu, Y.-H. Lin, W. H. Hui and C. C. Chang, Development of artificial compressibility solver in unified coordinates for moving body simulation, 18th AIAA Computational Fluid Dynamics Conference, AIAA-2007-4472, 25 - 28 Jun 2007, USA.
- [10] E. F. Toro, Riemann solvers for the incompressible Navier-Stokes equations, The Manchester Metropolitan University, Technical Report MMU 97-002, 1997.
- [11] A. Harten, P. D. Lax and B. van Leer, On upstream differencing and Godunov-type schemes for hyperbolic conservation law, *SIAM Review*, 25(1) (1983), 35-61.
- [12] P. Batten, M. A. Leschziner and U. C. Goldberg, Average-state Jacobians and implicit methods for compressible viscous and turbulent flows, *J. Comput. Phys.*, 137 (1997), 38-78.

- [13] E. F. Toro, M. Spruce and W. Spears, Restoration of the contact surface in the HLL Riemann solver, *Shock Wave*, 4 (1994), 25-34.
- [14] B. Einfeldt, C. D. Munz, P. L. Roe and B Sjøgreen, On Godunov-type methods near low densities, *J. Comput. Phys.*, 92 (1991), 273-296.
- [15] P. N. Shankar and M. D. Deshpande, Fluid mechanics in driven cavity, *Ann. Review Fluid Mech.*, 32 (2000), 93-136.
- [16] S. Garcia, The lid-driven square cavity flow: From stationary to time periodic and chaotic, *Commun. Comput. Phys.*, 2 (2007), 900-932.
- [17] U. Ghia, K. N. Ghia and C. T. Shih, High-resolutions for incompressible flow using Navier-Stokes equations and a multigrid method, *J. Comput. Phys.*, 48 (1982), 387-411.
- [18] M. E. DeBakey, D. A. Cooley and O. Creech Jr., Surgical consideration of dissecting aneurysm of the aorta, *Ann. Surgery*, 142 (1955), 586-592.
- [19] P. J. Kilner, Z. Y. Yang, R. H. Mohiaddin, D. N. Firmin and D. B. Longmore, Helical and retrograde secondary flow patterns in the aortic arch studied by three-dimensional magnetic resonance velocity mapping, *Circulation*, 88 (1993), 2235-2247.
- [20] D. Tang, C. Yang and D. N. Ku, A 3-D thin-wall model with flow-structure interactions for blood flow in carotid arteries with symmetric and asymmetric stenoses, *Comput. Struct.*, 72 (1999), 357-377.
- [21] Y. Qiu, and J. M. Tarbell, Numerical simulation of pulsatile flow in a compliant curved tube model of a coronary artery, *J. Biomech. Engr.*, 122 (2000), 77-85.
- [22] T. W. Taylor and T. Yamaguchi, Three-dimensional simulation of blood flow in an abdominal aortic aneurysm-steady and unsteady flow cases, *J. Biomech. Engr.*, 116 (1994), 89-97.
- [23] Y.-Y. Niu, W.-K. Chu, L.-C. Lee and H.-Y. Yu, Numerical evaluation of curvature effects on shear stresses across arterial stenoses, *J. Biomed. Engr. Appl., Basis Commun.*, 14(4) (2002), 164-170.
- [24] N. Shahcheragh, H. A. Dwyer, A. Y. Cheer, A. I. Barakat and T. Rutaganira, Unsteady and three-dimensional simulation of blood flow in the human aortic arch, *J. Biomech. Engr.*, 124 (2002), 77-85.